

Thesis Proposal

Erick Hernández Gutiérrez

October 24, 2022

Contents

1	Introduction	3
1.1	Diffusion MRI Background	3
1.2	Diffusion Tensor Imaging	3
1.3	Phantoms	4
1.3.1	Physical Phantoms	5
1.3.2	Digital Phantoms	5
1.4	State-of-the-art	6
1.4.1	Multiple Fascicle Reconstruction Methods	6
1.4.1.1	Diffusion Spectrum Imaging	7
1.4.1.2	Q-Ball Imaging	7
1.4.1.3	Diffusion Orientation Transform	8
1.4.1.4	Spherical Deconvolution Methods	8
1.4.1.5	Symmetric Tensor Decomposition	9
1.4.1.6	Diffusion Bases Functions	10
1.4.1.7	Multi-Tensor Methods	10
1.4.1.8	DIAMOND	11
1.4.2	Tractometry Pipelines	11
1.5	Problem Statement	12
1.6	Objective	13
2	Methods	14
2.1	Data	14
2.1.1	Synthetic Dataset	14
2.1.2	Myelo Inferno Dataset	17
2.2	Preprocessing	17
2.2.1	TractoFlow	17
2.2.2	ReconBundlesX	18
2.2.3	Rician Bias Correction	19
2.3	MRDS	19
2.4	Tractometry	20

CONTENTS	2
3 Results	21
3.1 Preliminary Results	21
3.1.1 Experiments on phantom	21
3.1.2 Experiments on myelo_inferno	21
3.2 Expected Results	21
3.2.1 Experiments on ms_6months	21
4 Research Activities	22
4.1 Expected Schedule	22
4.2 Conference Abstracts & Journal Publications	22
4.3 Collaborations	23
5 Conclusions	24

Chapter 1

Introduction

1.1 Diffusion MRI Background

1.2 Diffusion Tensor Imaging

The principal direction of diffusion in the tissue can be represented with a method called Diffusion Tensor Imaging (DTI). It was rigorously formalized for the first time in [11, 12, 13], which were pioneer works in the field. Assuming Gaussian diffusion, DTI builds the apparent water self-diffusion tensor at each voxel. The structure of the tensor allows to infer the orientation of the diffusion compartments within the voxel. For example, the major eigenvector of the tensor is parallel to the principal fiber orientation, see Figure 1.1.

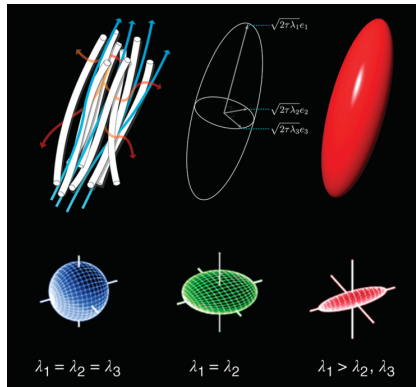


Figure 1.1: DTI ellipsoids, prolate, oblate, and spherical tensors. Water molecules diffusion along fibers. The diffusion tensor model captures this orientated diffusion process with the diffusion ellipsoid. Here, the FA of the illustrated tensor is approximately 0.7. The tensor can also be oblate if the first two eigenvalues are equal or spherical if all three are equal. Figure taken from [42].

The diffusion signal from a single Gaussian diffusion compartment within a voxel

is given by

$$E(\mathbf{g}_i, b) = \exp(-b\mathbf{g}_i^T \mathbf{D}\mathbf{g}_i), \quad 1 \leq i \leq n, \quad (1.1)$$

where E_i is the normalized diffusion signal magnitude for the DEO g_i , and \mathbf{D} is the apparent diffusion tensor mathematically written as a 3×3 symmetric and positive definite matrix

$$\mathbf{D} = \begin{pmatrix} D_{xx} & D_{xy} & D_{xz} \\ D_{yx} & D_{yy} & D_{yz} \\ D_{zx} & D_{zy} & D_{zz} \end{pmatrix}.$$

The diffusion tensor can be decomposed into its eigenvectors \mathbf{e}_1 , \mathbf{e}_2 and \mathbf{e}_3 and eigenvalues λ_1 , λ_2 and λ_3 using traditional matrix diagonalization methods or they can be obtained directly from the tensor values as it was documented in [14, 15, 16]. The largest eigenvector \mathbf{e}_1 gives the Principal Diffusion Direction (PDD) of the tensor. The rest of the eigenvectors determine the orthogonal planes to it, see Figure 1.1. These eigenvectors and eigenvalues not only determine the shape of the tensor, but they are closely related to brain tissue properties. For example, the largest eigenvalue λ_1 is equal to the Axial Diffusivity (AD), while $\frac{\lambda_2+\lambda_3}{2}$ give information about the Radial Diffusivity (RD). Besides, from the diffusion tensor eigenvalues, several spherical measures can be extracted such as the Mean Diffusivity (MD) $MD = \frac{\lambda_1+\lambda_2+\lambda_3}{3}$, Fractional Anisotropy (FA) $FA = \sqrt{\frac{(\lambda_1-\lambda_2)^2+(\lambda_1-\lambda_3)^2+(\lambda_2-\lambda_3)^2}{3(\lambda_1^2+\lambda_2^2+\lambda_3^2)}}$, among others. These measures have been widely used in publications within the field and constitute an important component for this work.

1.3 Phantoms

Either in neuroscience research or clinical applications, validation is a requirement. Estimation of the fiber tracts and tissue profiles is extremely challenging. Besides, it is well-known that there is not in-vivo data with a real ground truth (GT) that could be used for validation. An extensively and successfully substitute for in vivo GT is the use of synthetic phantoms. They constitute a controllable scenario that provides precise information of the underlying microstructural properties (e.g. local fiber orientation, geometrical configuration of fiber tracts, tissue properties, etc.). There are plenty of phantoms in the state-of-the-art that serve as validation tools for quantitatively and qualitatively evaluation of the performance of tractography [30] and microstructural estimation of diffusion MRI metrics [31]. Phantoms can be classified into two groups: physical and digital phantoms.

1.3.1 Physical Phantoms

It is possible to build hardware objects with arrangements of fibers crafted using synthetic, natural or glass fibers filled or soaked in a liquid [20, 21, 22, 23, 24, 25, 26, 27, 28, 29]. This emulates the water diffusion in restricted tissue. These phantoms can be imaged using a magnetic resonance scanner to get a diffusion-weighted signal because they are real world objects.



(a) Example of 90° and 45° physical phantoms resulting from a manual wiring of acrylic fibers (outer diameter of 17 μm) inside a container incorporating the negative mask of the target fiber bundles. Image taken from [20].

(b) Filling of a diffusion MRI tractography phantom under vacuum conditions and post-sonication to avoid the presence of air bubbles inside the fiber bundles. Image taken from [30].

Figure 1.2: Example of physical phantoms used for tractography validation.

1.3.2 Digital Phantoms

In contrast to physical phantoms, digital phantoms - also called numerical phantoms - are digital objects generated with a computer software. They consist of multiple components: (1) A structure model defining the simulated fiber configuration, (2) a diffusion model describing the water diffusion in the structural model, which determinates the signal attenuation in the diffusion-weighted signal, and (3) an algorithm that simulates the signal using the previous two components.



Figure 1.3: Illustration of the Phantomas phantom used for 2nd HARDI Reconstruction Challenge5, organized at ISBI 2013. It consists of 27 fiber bundles, on a $70 \times 70 \times 70$ grid, with 3 spherical CSF regions abstractly mimicking a human brain. Image taken from [30].

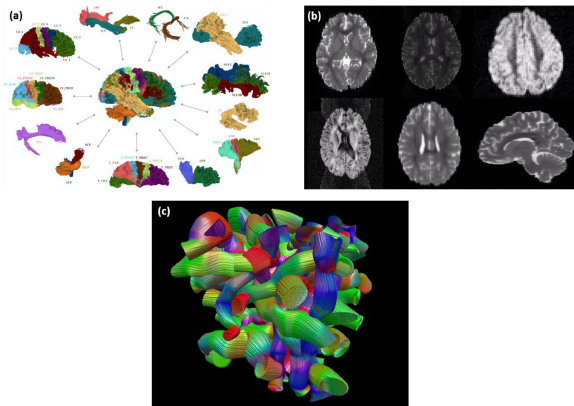


Figure 1.4: Illustration of the 71 tracts used for the 99 brains Fiberfox simulation (a), exemplary axial slices of one simulated subject of the 99 brains dataset with various artifacts (b), and an exemplary phantom with randomized bundle configuration generated using Fiberfox (c). Image taken from [30].

Both physical and digital phantoms have their own advantages and limitations according to the use-cases. The most important difference between them is that even with a well defined physical phantom, it is not possible to provide such a perfect ground truth because of, for example, mechanical limitations or the statistical nature of the diffusion process [30]. Hence, digital phantoms are the only way to obtain a dMRI data with a real ground truth. That's why we have decided to use a digital phantom for this work. We will discuss the selected phantom in the next chapter.

1.4 State-of-the-art

1.4.1 Multiple Fascicle Reconstruction Methods

Limitations of DTI came when several fiber populations are present in a voxel.

1.4.1.1 Diffusion Spectrum Imaging

Diffusion Spectrum Imaging (DSI) [10] is a MRI technique that employs the diffusion propagator p to describe the diffusion process in each voxel. It uses Fourier relationship between a, sufficient dense, cartesian sample of the signal S in the q-space and the diffusion probability density function such that

$$p(\vec{r}, t) = \mathcal{F}^{-1}\{S(\vec{q}, t)\} = \int_{\mathbb{Q}^3} S(\vec{q}, t) \exp(i\vec{q} \cdot \vec{r}) d\vec{q},$$

where \mathcal{F}^{-1} is the 3D inverse Fourier transform. Then, the dODF Ψ can be reconstructed by radially projecting $p(\vec{r}, t)$

$$\Psi(\hat{\mathbf{r}}) = \int_0^\infty p(r\hat{\mathbf{r}}, t) dr, \quad (1.2)$$

where $r \in \mathbb{R}_0^+$ and $\hat{\mathbf{r}} \in \mathbb{S}^2$. DSI can detect the multiple fascicle orientation within a voxel. However, it requires strong gradients ($0 \leq b \leq 20,000 \text{ s/mm}^2$) as well as long acquisition time to measure hundreds of directions and b-values. That's why is of real interest in clinical applications.

1.4.1.2 Q-Ball Imaging

The Q-Ball Imaging (QBI) is a method that employ the Funk-Radon transform (FRT) on HARDI derived data to obtain a diffusion ODF (dODF)

$$\Psi(\hat{\mathbf{u}}) = \int_{\Omega(\hat{\mathbf{u}})} S(\hat{\mathbf{q}}, t) d\hat{\mathbf{q}},$$

where $\Omega(\hat{\mathbf{u}}) = \{\hat{\mathbf{q}} \in \mathbb{S}^2 \mid \hat{\mathbf{q}} \perp \hat{\mathbf{u}}\}$, $\hat{\mathbf{q}} = \mathbf{q}/q$ and $\mathbf{q} \in \mathbb{Q}^3$. FRT uses the fact that the diffusion signal $S(\hat{\mathbf{q}}, t)$ is maximal in the directions perpendicular to the underlying fascicles, see Figure 1.5. The dODF can properly represent the presence and orientation of multiple crossing fascicles. However, the resulted dODF is artificially smooth and inflated compared to the true diffusion ODF. Problematically, this same feature causes QBI to poorly distinguish fibers crossing at tight angles. Some modifications and generalizations to QBI have been published to try to achieve most of the QBI limitations [39, 40, 41].

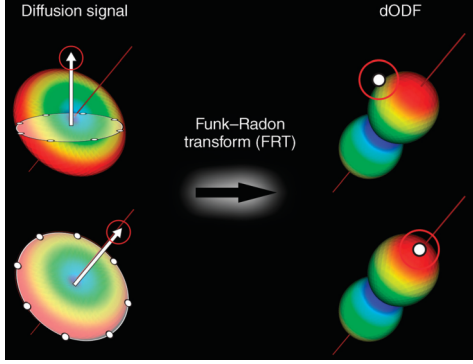


Figure 1.5: Illustration of the FRT that QBI uses to reconstruct the dODF using the diffusion MRI measured signal. Image taken from [42].

1.4.1.3 Diffusion Orientation Transform

The Diffusion Orientation Transform (DOT) [36] is a technique that provides a direct estimation of displacement probability surfaces at each voxel from the dMRI data. DOT uses the Fourier relationship between the signal attenuation and the diffusion propagator p

$$p(\vec{r}, t) = \oint_{\mathbb{S}^2} \int_0^\infty E(\mathbf{q}, t) \exp(-2\pi i r q \hat{\mathbf{q}}^T \hat{\mathbf{r}}) q^2 dq d\hat{\mathbf{q}}, \quad (1.3)$$

where $\mathbf{q} = q\hat{\mathbf{q}} \in \mathbb{Q}^3$ and $\hat{\mathbf{r}} = r\hat{\mathbf{r}}$. It is assumed that E attenuates mono-exponentially, i.e. $E(\mathbf{q}, t) = \exp(-4\pi^2 t q^2 D(\hat{\mathbf{q}}))$, where D is the apparent diffusion coefficient or diffusivity profile. In other words, DOT transforms water diffusivity profiles into displacement probability profiles. Finally, the dODF can be obtained from $p(\vec{r}, t)$ by means of the radial projection as in Equation 1.2. DOT faces some limitations regarding the HARDI sampling schemes with finite support, truncated spherical harmonics and the mono-exponential attenuation. In [37] was proposed an extension of the DOT method that mitigates these limitations.

1.4.1.4 Spherical Deconvolution Methods

Spherical Deconvolution (SD) [33] is one of the most popular techniques to recover the principal diffusion directions from the dMRI data. SD considers the HARDI signal S as the convolution of the response function, which is an axially symmetric kernel R that represents a single-fiber response, with the expected true fiber Orientation Distribution Function F , known as fODF. Given the measurements of S along all the n gradient directions, the fODF can be reconstructed by solving the following optimization problem

$$\min_F \frac{1}{2} \sum_{i=1}^n \|S(\mathbf{g}_i, b) - S_0 \int_{\mathbb{S}^2} F(\mathbf{v}) R(\mathbf{g}_i, \mathbf{v}) d\mathbf{v}\|^2, \quad (1.4)$$

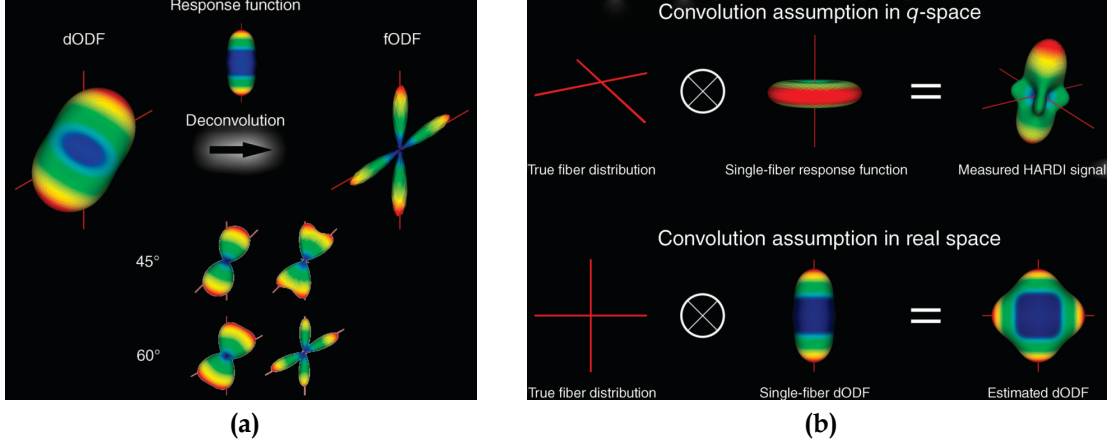


Figure 1.6: Imagen taken from [42].

This SD technique is ill-posed and affected by noise. Later in [34] was introduced a modification to SD called Constrained Spherical Deconvolution (CSD) that preserves the angular resolution while remaining robust to noise effects. In CSD a non-negativity constraint on the estimated fODF is included into the formulation, as negative fibre orientation densities are physically impossible. Besides, this constraint eliminates the need for low-pass filtering the obtained fODF. In order to perform the deconvolution over the sphere, the spherical representation $S(\theta, \phi)$ of S can be written as

$$S(\theta, \phi) = F(\theta, \phi) \otimes R(\theta)$$

1.4.1.5 Symmetric Tensor Decomposition

Symmetric Tensor Decomposition (STD) [32] combines the fODF reconstruction of SD and the orientations approximation into one optimization problem. It approximates the fODF using an equivalent lower-rank approximation by a symmetric tensor decomposition

$$F(\mathbf{v}) \simeq \sum_{i=1}^{\tilde{r}} \gamma_i f_i^d = \sum_{i=1}^{\tilde{r}} (\boldsymbol{\alpha}_i \cdot \mathbf{v})^d, \quad \tilde{r} < r, \boldsymbol{\alpha}_i \in \mathbb{R}^3, \mathbf{v} \in \mathbb{S}^2.$$

Combining this with the SD approach of Equation 1.4 we obtain the following non-linear optimization problem

$$\min_{\boldsymbol{\alpha}_j} \frac{1}{2} \sum_{i=1}^n \|S(\mathbf{g}_i, b) - S_0 \int_{\mathbb{S}^2} (\boldsymbol{\alpha}_i \cdot \mathbf{v})^d R(\mathbf{g}_i, \mathbf{v}) d\mathbf{v}\|^2 \quad (1.5)$$

1.4.1.6 Diffusion Bases Functions

Diffusion Bases Functions (DBF) is a dictionary-based method for the estimation of the intra-voxel configuration [7]. A set $\{\Phi_j\}_{j=1}^J$ of J basis functions are generated using the radially symmetric diffusion tensor. Then, the diffusion signal S can be expressed in matrix form

$$S = \Phi\alpha, \quad (1.6)$$

where $S = (S(\mathbf{g}_1, b), \dots, S(\mathbf{g}_n, b)) \in \mathbb{R}^n$ is the vector of diffusion signal samples, $\alpha \in \mathbb{R}^J$ is the vector of contributions for each basis function and $\Phi \in \mathbb{R}^{n \times J}$ is the dictionary containing all J basis functions of size n .

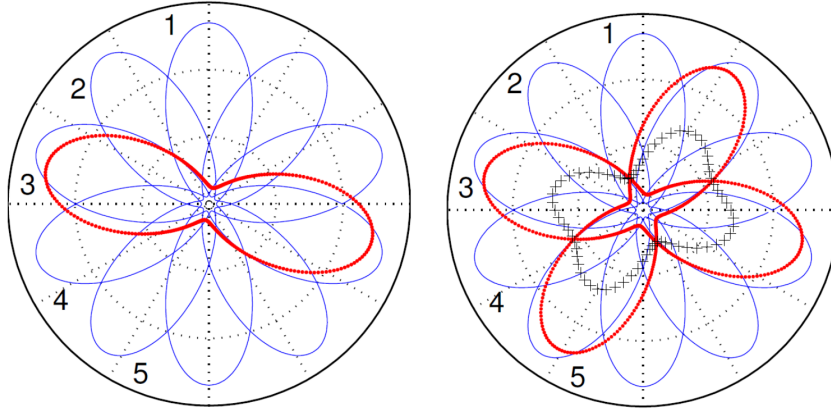


Figure 1.7: 2D schema of DBFs. The blue lines correspond to a dictionary with $J = 5$ basis functions. (a) Continuous-blue line shows the DBFs generated by an uniformly distributed tensor basis with $J = 5$. The doted-red line represents the normalized diffusion signal $S(\mathbf{q})$ generated by an arbitrary diffusion tensor. In this case, the solution for α is expected to be $\alpha = (0, 0, 1, 0, 0)$. (b) Schema for two fiber case, the dotted-red lines represent the signals for two arbitrary tensors, which their half-addition of both signals are shown in the cross-marked black line. For this case, the solution is expected to be $\alpha = (0, 0, 0.5, 0, 0.5)$. Image taken from [7].

Finally, Equation 1.6 is solved for α using a basis pursuit technique, which compute the solution by means of non-negative least-squares of the form

$$\min_{\alpha} \|\alpha\|_1 = \sum_j \alpha_j \quad \text{subject to } S = \Phi\alpha, \quad \alpha_j \geq 0, \quad j = 1, \dots, J.$$

1.4.1.7 Multi-Tensor Methods

Multi-tensor representation or Multi-tensor Model (MTM) is a natural extension of DTI, where orientated diffusion along the fascicles is represented with a mixture

of Gaussian distributions at each voxel such that

$$E(\mathbf{g}_i, t) = \sum_{k=1}^N \alpha_k \exp(-b\mathbf{g}_i^T \mathbf{D}_k \mathbf{g}_i). \quad (1.7)$$

Initially, the expectation maximization algorithm was used to solve Equation 1.7. However, this algorithm is unable to handle physiological constraints on the eigenvalues. Later, in [1] a gradient descent scheme with multiple restarts was employed to solve, by considering the mentioned constraints, the Equation 1.7 for the eigenvectors of \mathbf{D}_k and volume fractions α_k , while the eigenvalues of \mathbf{D}_k were specified a priori or restricted to a particular range. However, these and others [2, 3, 4] proposed methods to solve the MTM have been reported to be numerically challenging and unstable. Later, in [8] was provided the first analytical demonstration that when using a diffusion MRI acquisition with only one non-zero b-value, such as in conventional single-shell HARDI acquisition, a co-linearity in model parameters makes the precise model estimation impossible.

1.4.1.8 DIAMOND

DIAMOND stands for Characterizing the DIistribution of Anisotropic MicrO-structural eNvironments with Diffusion-weighted imaging (DIAMOND) [9]. This method consider that the measured signal can be described by a sum of signals arising from a large number of individual spin-packets within the voxel. Each spin-packet undergoes homogeneous 3D Gaussian diffusion represented by a diffusion tensor \mathbf{D} , whose contribution to the signal for a DEO \mathbf{g}_i is

$$S_0 \exp(-b_i \mathbf{g}_i^T \mathbf{D} \mathbf{g}_i) d\mathbf{D}.$$

A matrix-variate distribution $P(\mathbf{D})$ determinates the fraction of spin-packets described by a same tensor \mathbf{D} . Thus, the DIAMOND representation is given by

$$S(\mathbf{g}_i, t) = S_0 \int_{\mathbb{D}} P(\mathbf{D}) \exp(-b_i \mathbf{g}_i^T \mathbf{D} \mathbf{g}_i) d\mathbf{D}, \quad (1.8)$$

where \mathbb{D} is the set of symmetric positive-definite 3×3 matrices. When a voxel is composed of one single fascicle, Equation 1.8 matches with DTI.

1.4.2 Tractometry Pipelines

When tractography reconstructions and metrics derived from diffusion quantification are combined, the term “tractometry” is used [55, 56]. In tractometry, diffusion metrics are typically averaged over the tracts of interest, see Figure 1.8.

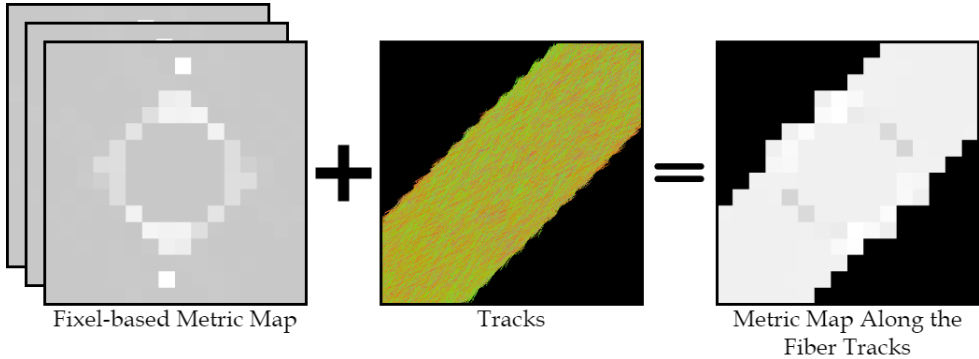


Figure 1.8: The fixel-based metric map has an image per every direction. Tractometry Illustration. The voxel value of the rightest image is the mean of the values of the metric map

The analysis of these metrics along the tracts is called “tract profiles” [57, 58, 59]. There are 2 types of tractometry reported in the literature: One that considers metrics derived from dMRI, while the others consider metrics from modalities other than dMRI.

1.5 Problem Statement

A major drawback to current methods like DSI, QBI, DOT and SD is that they focus on describing the general shape of the diffusion profile in each voxel instead of representing each fascicle independently, and therefore they do not enable characterization of each individual fascicle. Hence, they provide information only about the orientation of crossing fascicles but not about the microstructure.

The metrics usually extracted from DTI, i.e. AD, RD, as well as their derivations such that MD and FA, tend to lack specificity to characterize the underlying microstructure, and are very sensitive to white matter anomalies []. Although RD is suggested as the closest biomarker of demyelination [64], none of them have proven to be a specific imaging biomarker of myelin. Besides, despite the notable available tractometry pipelines in the state-of-the-art, all methods are based on dMRI metrics from single tensor. It is thus clear that it is important to study a tractometry pipeline informed with fixel-based dMRI metrics like fixel-RD, which aims to achieve the crossing fiber limitations of single tensor derived dMRI metrics. Fixel-based analysis needs to be translated to neurodegenerative diseases and this is still a very important open problem.

1.6 Objective

Our main objective is to setup a robust (to noise and crossing fibers) pipeline for the automatic extraction and statistical analysis of track-specific white matter measures. Estimated fixel-based orientations and metrics will be used as indirect proxies to axon loss, demyelination and neuroinflammation. In particular, the fixel-based RD (fixel-RD) could help to account for demyelination in MS patients as in [54]. In order to achieve this, there are two main problems that have to be addressed:

1. Fast, accurate and robust to noise and fiber crossing voxel-wise estimation of fixel-based metrics in diffusion MRI signal using the multi-tensor based method MRDS. This demands to improve the model selector step in MRDS to better estimate the number of tensors per voxel. Besides, parallelization of MRDS is necessary to ensure fast fitting of the MRDS method to the diffusion MRI signals.
2. Multimetric analysis of white matter tracts in different fiber bundles. It's required to adapt the tractometry_flow pipeline to integrate the MRDS metrics into the statistical analysis.

Although automating tract-profiling and metrics for white matter could improve brain connectivity mapping through crossing fiber regions and pathologies in the human brain, we will focus to demonstrate the application of our pipeline to multiple sclerosis (MS) disease.

Chapter 2

Methods

2.1 Data

2.1.1 Synthetic Dataset

In order to validate the performance of the proposed method in complex scenarios, we opted for the digital phantom from the ISBI 2012 - HARDI Reconstruction Workshop [17, 18]. This phantom has an structure field with specific arrangements of synthetic fibers that mimic challenging crossing configurations. The structure of the phantom consists of a $16 \times 16 \times 5$ voxels and 3 fiber bundles with a 3D configuration of tracts, see Figure 2.1. The phantom has been used before to evaluate and compare a large selection of reconstruction algorithms for recovering the local intra-voxel fiber structure from diffusion MRI acquisitions [17].

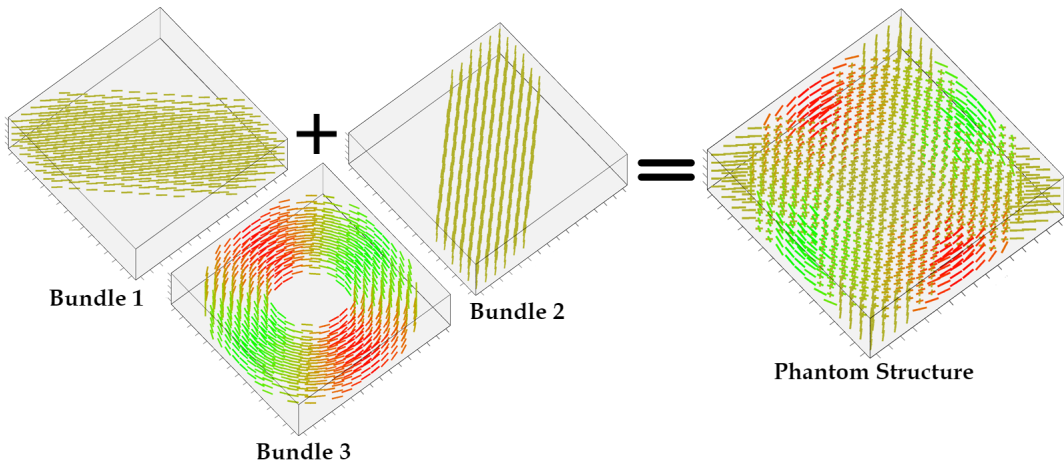


Figure 2.1: The structured field of the digital phantom showing the 3 fiber bundles configuration. The directions of the fiber populations are colored depending on their orientation using the color code $(x, y, z) \rightarrow (r, g, b)$.

The simulation of the diffusion-weighted signal intensity was numerically simulated in every voxel by adopting the classical Gaussian mixture representation described in Equation 1.7:

$$S(\mathbf{q}) = S_0 \sum_{k=1}^N \alpha_k \exp(-b\mathbf{g}_i^T \mathbf{D}_k \mathbf{g}_i),$$

where $\mathbf{q} \in \mathbb{Q}^3$ is the vector in q-space corresponding to the DEO $\mathbf{g}_i \in \mathbb{S}^2$, b-value b and diffusion time t with $\mathbf{q} = q\mathbf{g}_i = \|\mathbf{q}\| \mathbf{g}_i$ and $b = 4\pi^2 q^2 t$. For the DEOs $\{\mathbf{g}_i\}_{i=1}^n$ and the b-values b the Penthera3T adquisition protocol [19] was used, which has 3 different shells $b = 300, 1000, 2000 \text{ mm}^2/\text{s}$ with 8, 32 and 60 directions, respectively, and 7 $b = 0$ for a total of $n = 107$ directions. Each bundle is determinated by the tensor \mathbf{D}_k , which is given by Equation 2.3. Assuming axial symmetry, eigenvalues $\lambda_{k,1}, \lambda_{k,2}$ and $\lambda_{k,3}$ of \mathbf{D}_k are the diffusivities along the parallel axis of the main diffusion $\lambda_k^\parallel = \lambda_1$ and the perpendicular axis $\lambda_k^\perp = (\lambda_2 + \lambda_3)/2$. In the original phantom proposed in the challenge, diffusivities were generated from ranges typically observed in the human brain: $\lambda_{k,1} \in [1, 2] \times 10^{-3} \text{ mm}^2/\text{s}$ and $\lambda_{k,2} = \lambda_{k,3} \in [0.1, 0.6] \times 10^{-3} \text{ mm}^2/\text{s}$. However, we injected lambda values directly estimated from the myelo_inferno dataset.

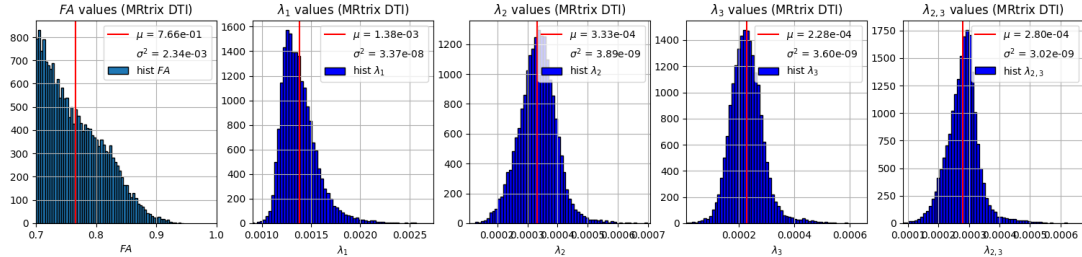


Figure 2.2: Histogram of lambda values estimated by fitting the DTI implementation included in MRtrix [48] to the myelo_inferno dataset.

The diffusion properties are constant along the trajectories. The signal S has been perturbed as in the original phantom by adding Rician noise such that

$$\tilde{S}(\mathbf{q}) = \sqrt{(S(\mathbf{q}) + \eta_1)^2 + \eta_2^2},$$

with $\eta_1, \eta_2 \sim \mathcal{N}(0, \sigma^2)$ and $\sigma = S_0/SNR$. We set the **signal-to-noise ratio (SNR)** to $SNR = 12$ to simulate challenging levels of noise. In [18] a MATLAB script for simulating the signal was proportioned. However, we made a faster and more flexible re-implementation of this script in Python. Instead of using an iterative approach, we used vectorized operations to speed the simulation. This improvement in performance allowed to include a new feature to add dispersion to the signal. Besides, we modified how the phantom receives the input parameters.

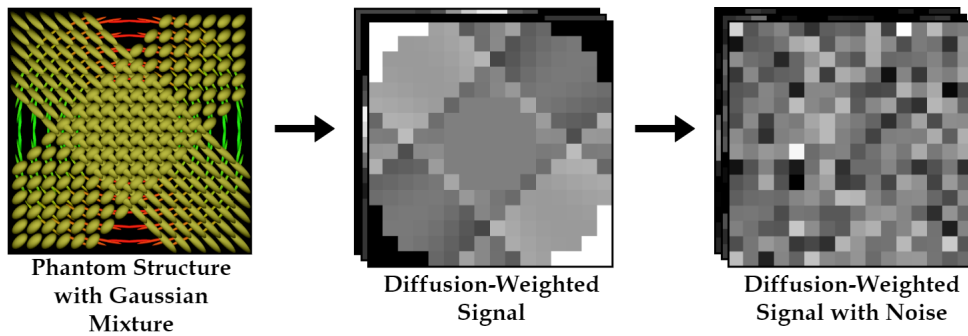


Figure 2.3: From phantom structure and Gaussian mixture to diffusion-Weighted signal with noise.

For example, lambda values are loaded from an input Nifti image instead of being hard coded in the script. This enables the possibility to simulate damage in the tracts by altering lambda values with a mask in a specific spot, see Figure 2.4. For the porpuse of this work, we generated two different datasets to simulate two different experimental conditions: healthy and demyelinated fiber tracts.

1. Control phantom subjects: without any damage and with lambda values similar to the control subjects of the myelo_inferno dataset. These subjects will be “healthy” subjects.
2. MS phantom subjects: with localized “damage” simulating demyelination, i.e. spots in the bundle with increased RD values, and hence lower overall FA and MD values. This is of special interest considering the localized nature of MS lesions.

Both datasets have 26 subjects to match the number of subjects in the myelo_inferno dataset.

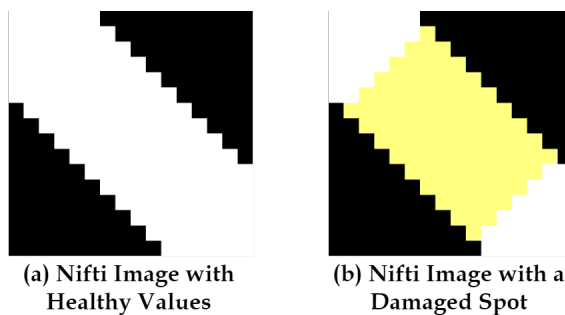


Figure 2.4: (a) Nifti image with control values (white) for the diffusivities of the Bundle 1. Values are constant along the bundle. (b) Nifti image for Bundle 1 with damage (yellow) values.

2.1.2 Myelo Inferno Dataset

The acquisitions were done by the Sherbrooke onnectivity Imaging Lab (SCIL). Twenty six young and healthy subjects (75% women and 25% men) were scanned six times. The DWI (112x112 matrix, TR 5615 ms, TE 95 ms, SENSE factor of 2) were acquired on a 3 Tesla MRI (Philips, Ingenia) with a single-shot echo-planar imaging sequence having 3 different shells, $b = 300, 1000, 2000\text{mm}^2/\text{s}$ with respectively 8, 32 and 60 directions distributed, 7 $b = 0$ for a total of 107 images and a 2mm isotropic spatial resolution. A reversed phase encoded $b=0$ image is available, to correct EPI distortions, with the same spatial resolution as the DWI. The T1-weighted MPRAGE image (TR 7.9ms, TE 3.5ms) has a 1mm isotropic spatial resolution.

2.2 Preprocessing

2.2.1 TractoFlow

Tractoflow [49] is a pipeline as nextflows that allows to analyse a whole dataset of diffusion MRI data in only one simple script. TractoFlow pipeline consist of 23 different steps: 14 steps for the diffusion weighted image processing and 8 steps for the T1 weighted image processing, see Figure 2.5.

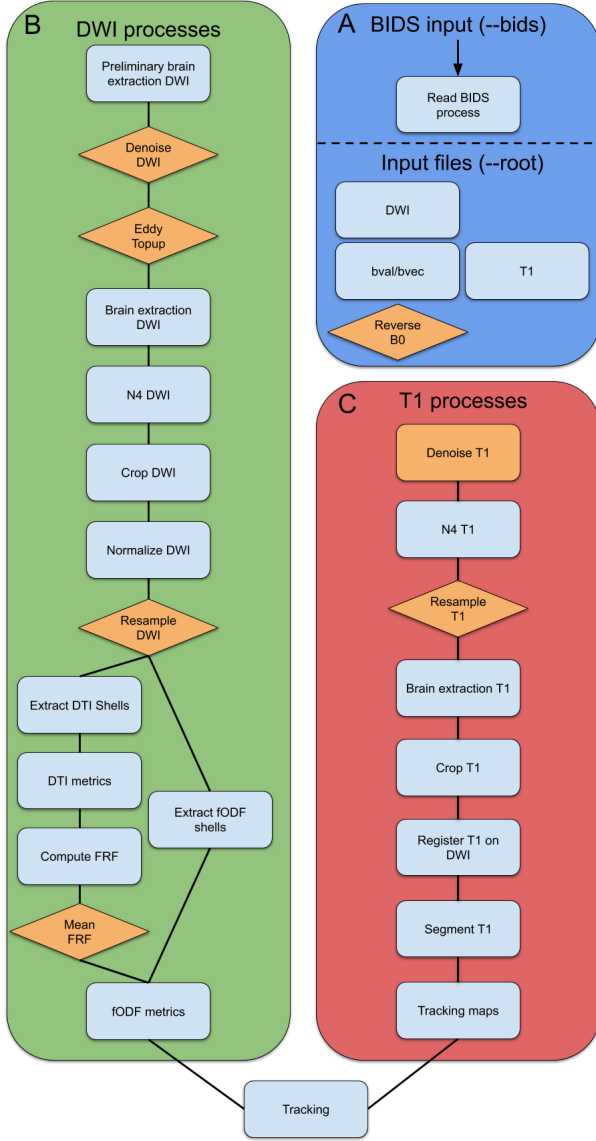


Figure 2.5: Processes of the TractoFlow pipeline. In A (blue), the input files required to run the pipeline. In B (green), the DWI processes that take the DWI, the b-values/b-vectors files and the reversed phase encoded $b = 0$ image. In C (red), the T1 processes that take the T1 weighted image in input. In orange, all processes or images that are optional. Image taken from [49].

2.2.2 ReconBundlesX

Once Tractoflow reconstructs a complete tractogram, the next step is to perform bundle recognition, where the entire tractogram is decomposed into separate bundles. Tractography streamlines are classified as either belonging to a particular

bundle or discarded. For this bundle segmentation, we use the ReconBundlesX flow (https://github.com/scilus/rbx_flow). ReconBundlesX is a tool to separate a wholebrain tractogram into different bundles divided into separate files [50, 51, 52, 53]. It is multi-atlas and multi-parameter, and more robust to the single atlases and single parameter version of RecoBundles published in DIPY [47] as it has been shown in [50].

2.2.3 Rician Bias Correction

Gudbjartsson correction

2.3 MRDS

The most appropriate representation and modeling of multiple fascicles traversing the same voxel remains unclear. Actually, there is a multi-tensor based method, which represents multiple fascicles with multi-tensors fitted using the **Multi Resolution Discrete Search (MRDS)** approach [6]. MRDS is capable of providing individual diffusion profiles as well as the orientation of the fascicles. MRDS is a general framework for estimating parameters in a multi-compartment representation. The normalized DWI signal attenuation $E_i = S_i/S_0$ at each voxel of a multi-compartment model is represented as

$$E_i = \sum_{k=1}^N \alpha_k \Phi_i(\zeta_k) + \eta_i, \quad i = 1, 2, \dots, n, \quad (2.1)$$

where N is the number of compartments, n the number of DEOs, $\{\alpha_k > 0\}_{k=1}^N$ denotes the compartment sizes (volume fractions) and η_i represents the signal noise. Besides, $\Phi_i(\zeta_k)$ is the signal response of the compartment function for the DEO g_i defined by the parameters ζ_k , which is a vector in the form $\zeta_k = (\theta_k, \xi_k)$, where $\theta_k = (\theta_k^z, \theta_k^a)$ define the zenith (elevation) and azimuth angles of the PDD of the compartment. On the other hand, ξ_k is the vector of parameters associated with the tissue properties for the compartment k . Assuming Gaussian noise, the error function to be minimized is

$$\epsilon(N, \alpha, \theta, \xi, E) = \sum_{i=1}^n \left(\sum_{k=1}^N \alpha_k \Phi_i(\zeta_k) - E_i \right)^2 \quad (2.2)$$

Note that in the particular case of a **multi-tensor model (MTM)** representation we have $\Phi_i(\zeta_k) = \exp(-b_i g_i^T D_k g_i)$, where $\xi_k = (\lambda_k^{\parallel}, \lambda_k^{\perp})$ represents the axial (\parallel) and radial (\perp) diffusivities. The PDD θ_k defines the rotation matrix $R(\theta_k)$ associated with D_k such that

$$D_k = D(\theta_k, \xi_k) = R(\theta_k) \begin{bmatrix} \lambda_k^{\parallel} & 0 & 0 \\ 0 & \lambda_k^{\perp} & 0 \\ 0 & 0 & \lambda_k^{\perp} \end{bmatrix} R^T(\theta_k). \quad (2.3)$$

Therefore, the proposed MRDS algorithm consists in the following steps:

1. Estimation of the orientations $\{\theta_k\}_{k=1}^N$ and the compartment sizes $\{\alpha_k\}_{k=1}^N$ for fixed diffusion parameters $\{\xi_k\}_{k=1}^N$.
2. Estimation of the diffusion parameters $\{\xi_k\}_{k=1}^N$ for fixed $\{\theta_k\}_{k=1}^N$ and $\{\alpha_k\}_{k=1}^N$.
3. Repeat previous steps until convergence.
4. The output of the previous steps consists of the best possible configurations for 1, 2 and 3 fascicle orientations and diffusivities. Finally, in this step a model selector determinates the optimal value for the number of bundles for the considered voxel.

MRDS has proved to be more robust to noise and crossing fascicles than other methods like DIAMOND and CSD [5].

2.4 Tractometry

The basis of tractometry is the statistical analysis that compares different groups or assesses individual variability in brain connection structure [60].

The nextflow-based tractometry pipeline called tractometry_flow [61, 62, 63] allows you to extract tractometry information by combining subjects' streamline bundles and diffusion MRI metrics. Adapting this pipeline to integrate the MRDS estimated metrics could allow us to recover a fixel-FA, fixel-MD, fixel-AD and, more importantly, fixel-RD per fiber bundle.

Chapter 3

Results

3.1 Preliminary Results

3.1.1 Experiments on phantom

3.1.2 Experiments on myelo_inferno

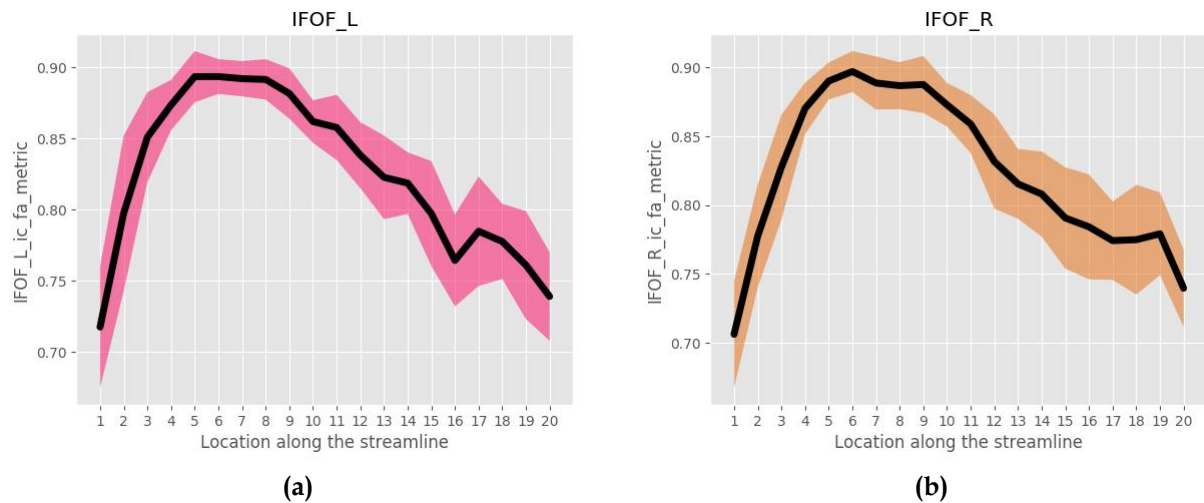


Figure 3.1: Results of the tractometry_flow on the myelo_inferno dataset along the IFOF fiber bundle.

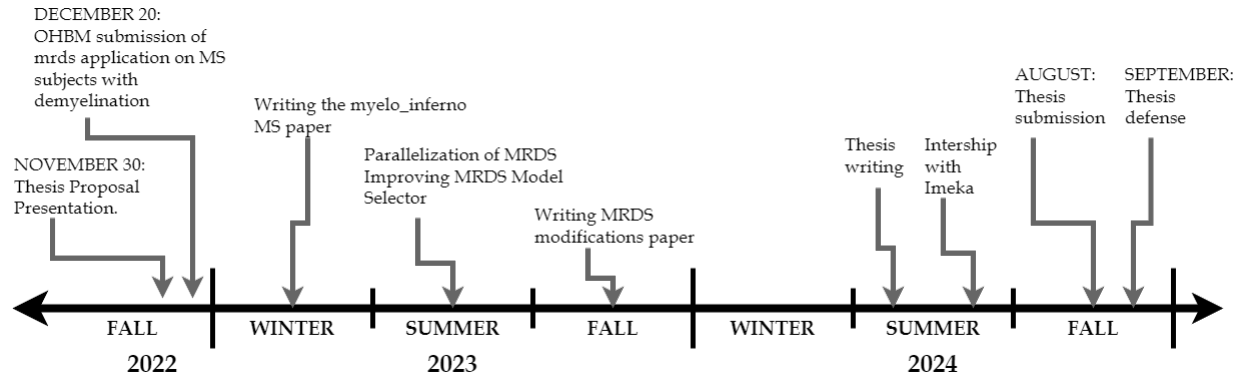
3.2 Expected Results

3.2.1 Experiments on ms_6months

Chapter 4

Research Activities

4.1 Expected Schedule



4.2 Conference Abstracts & Journal Publications

- Robust Estimation of Fascicle-based Fractional Anisotropy on Fiber Crossings [43].
- Tractography from Gaussian multi-compartmental ODFs [44].
- Structural connectivity estimates are accurate: the outcome of diffusion-simulated connectivity (DiSCo) challenge [45].
- Real-Time Rendering of Massive Multi-Tensor Fields Using Modern OpenGL [46].
- MRDS optimization
- results of the study using MRDS and tractometry_flow on the myelo_inferno.

4.3 Collaborations

- Imeka** Intership with Imeka Solutions Inc.; a company specialized in brain imaging specifically white matter, neuroinflammation, free-water and more. We will develop mechanisms and modify others already in place to integrate the MRDS-based pipeline into the Imeka's software infrastructure. This could enable the ability to test the pipeline on large public and clinical Imeka databases with more than 5,000 MRI exams (Duration: 3-6 months).
- NYU** Collaboration with the NYU MRI Biophysics Group, which is one of the most relevant laboratories in the field. It will focus on multimetric analysis of white matter tracts in the multi-compartment standard model (Duration: 3-6 months).

Chapter 5

Conclusions

No conclusions yet...

Bibliography

- [1] Tuch DS, Reese TG, Wiegell MR, Makris N, Belliveau JW, Wedeen VJ. High angular resolution diffusion imaging reveals intravoxel white matter fiber heterogeneity. *Magn Reson Med.* 2002 Oct;48(4):577-82. doi: 10.1002/mrm.10268. PMID: 12353272.
- [2] Hosey T, Williams G, Ansorge R (2005) Inference of multiple fiber orientations in high angular resolution diffusion imaging. *Magn Reson Med* 54: 1480–1489.
- [3] Kreher BW, Schneider JF, Mader I, Martin E, Hennig J, et al. (2005) Multitensor approach for analysis and tracking of complex fiber configurations. *Magn Reson Med* 54: 1216–1225.
- [4] Melie-Garcia L, C-Rodriguez EJ, Aleman-Gomez Y, Lin CP, Iturria-Medina Y, et al. (2008) A Bayesian framework to identify principal intravoxel diffusion profiles based on diffusion-weighted MR imaging. *Neuroimage* 42: 750–770.
- [5]
- [6]
- [7] Ramirez-Manzanares, M. Rivera, B. C. Vemuri, P. Carney, and T. Mareci. Diffusion basis functions decomposition for estimating white matter intravoxel fiber geometry. *IEEE Transactions on Medical Imaging*, 26(8):1091–1102, 2007.
- [8]
- [9]
- [10]
- [11] Basser PJ, Mattiello J, Turner R, Le Bihan D. Diffusion tensor echo-planar imaging of human brain. InProceedings of the SMRM 1993 Aug (Vol. 584).
- [12] Basser PJ, Mattiello J, Le Bihan D. Estimation of the effective self-diffusion tensor from the NMR spin echo. *J Magn Reson* 1994; 103: 247–254.

- [13] Basser PJ, Mattiello J, Le Bihan D. MR diffusion tensor spectroscopy and imaging. *Biophys J* 1994; 66: 259–267.
- [14]
- [15]
- [16]
- [17]
- [18] http://hardi.epfl.ch/static/events/2012_ISBI/download.html
- [19] <https://zenodo.org/record/2602049#.Y1UzCHaZNPY>
- [20] C. Poupon, B. Rieul, I. Kezele, M. Perrin, F. Poupon, J.F. Mangin New diffusion phantoms dedicated to the study and validation of high-angular-resolution diffusion imaging (HARDI) models *Magn. Reson. Med.*, 60 (2008), pp. 1276-1283, 10.1002/mrm.21789.
- [21] J. D. Tournier, C. H. Yeh, F. Calamante, K. H. Cho, A. Connelly, and C. P. Lin, “Resolving crossing fibres using constrained spherical deconvolution: Validation using diffusion-weighted imaging phantom data,” *NeuroImage*, vol. 42, pp. 617–625, 2008.
- [22] F. B. Laun, L. R. Schad, J. Klein, and B. Stieltjes, “How background noise shifts eigenvectors and increases eigenvalues in DTI,” in *MAGMA*, 2009, vol. 22, pp. 151–158.
- [23] F. B. Laun, S. Huff, and B. Stieltjes, “On the effects of dephasing due to local gradients in diffusion tensor imaging experiments: Relevance for diffusion tensor imaging fiber phantoms,” *Magn. Reson. Imag.*, vol. 27, pp. 541–548, 2009.
- [24] P. Pullens, A. Roebroeck, and R. Goebel, “Ground truth hardware phantoms for validation of diffusion-weighted MRI applications,” *J. Magn. Reson. Imag.*, vol. 32, pp. 482–488, 2010.
- [25] K. H. Fritzsche, F. B. Laun, H. P. Meinzer, and B. Stieltjes, “Opportunities and pitfalls in the quantification of fiber integrity: What can we gain from Q-ball imaging?,” *NeuroImage*, vol. 51, pp. 242–251, 2010.
- [26] A. Moussavi-Biugui, B. Stieltjes, K. Fritzsche, W. Semmler, and F. B. Laun, “Novel spherical phantoms for Q-ball imaging under in vivo conditions,” *Magn. Reson. Med.*, vol. 65, pp. 190–194, 2011.

- [27] F. L. Zhou, P. L. Hubbard, S. J. Eichhorn, and G. J. Parker, "Coaxially electrospun axon-mimicking fibers for diffusion magnetic resonance imaging," *ACS Appl. Mater Interfaces*, vol. 4, pp. 6311–6316, 2012.
- [28] T. A. Kuder, B. Stieltjes, P. Bachert, W. Semmler, and F. B. Laun, "Advanced fit of the diffusion kurtosis tensor by directional weighting and regularization," *Magn. Reson. Med.*, vol. 67, pp. 1401–1411, 2012.
- [29] M. Bach, K. H. Fritzsche, B. Stieltjes, and F. B. Laun, "Investigation of resolution effects using a specialized diffusion tensor phantom," *Magn. Reson. Med.*, 2013.
- [30] Ivana Drobniak, Peter Neher, Cyril Poupon, Tabinda Sarwar, Physical and digital phantoms for validating tractography and assessing artifacts, *NeuroImage*, Volume 245, 2021, 118704, ISSN 1053-8119, <https://doi.org/10.1016/j.neuroimage.2021.118704>.
- [31] Els Fieremans, Hong-Hsi Lee, Physical and numerical phantoms for the validation of brain microstructural MRI: A cookbook, *NeuroImage*, Volume 182, 2018, Pages 39-61, ISSN 1053-8119, <https://doi.org/10.1016/j.neuroimage.2018.06.046>.
- [32]
- [33]
- [34]
- [35]
- [36]
- [37]
- [38]
- [39]
- [40]
- [41]
- [42]
- [43]
- [44]
- [45]

- [46]
- [47] Garyfallidis E, Brett M, Amirbekian B, Rokem A, van der Walt S, Descoteaux M, Nimmo-Smith I; Dipy Contributors. Dipy, a library for the analysis of diffusion MRI data. *Front Neuroinform.* 2014 Feb 21;8:8. doi: 10.3389/fninf.2014.00008. PMID: 24600385; PMCID: PMC3931231.
- [48] Tournier, J.-D.; Smith, R. E.; Raffelt, D.; Tabbara, R.; Dhollander, T.; Pietsch, M.; Christiaens, D.; Jeurissen, B.; Yeh, C.-H. & Connelly, A. MRtrix3: A fast, flexible and open software framework for medical image processing and visualisation. *NeuroImage*, 2019, 202, 116137
- [49] Theaud, G., Houde, J.-C., Boré, A., Rheault, F., Morency, F., Descoteaux, M., TractoFlow: A robust, efficient and reproducible diffusion MRI pipeline leveraging Nextflow & Singularity, *NeuroImage*, <https://doi.org/10.1016/j.neuroimage.2020.116889>
- [50] Rheault, Francois. Analyse et reconstruction de faisceaux de la matière blanche. page 137-170, (2020), <https://savoirs.usherbrooke.ca/handle/11143/17255>
- [51] Garyfallidis, Eleftherios, et al. Recognition of white matter bundles using local and global streamline-based registration and clustering. *NeuroImage* 170 (2018) <https://doi.org/10.1016/j.neuroimage.2017.07.015>
- [52] Kurtzer GM, Sochat V, Bauer MW Singularity: Scientific containers for mobility of compute. *PLoS ONE* 12(5): e0177459 (2017) <https://doi.org/10.1371/journal.pone.0177459>
- [53] P. Di Tommaso, et al. Nextflow enables reproducible computational workflows. *Nature Biotechnology* 35, 316–319 (2017) <https://doi.org/10.1038/nbt.3820>
- [54] Dayan M, Monohan E, Pandya S, Kuceyeski A, Nguyen TD, Raj A, Gauthier SA. Profilometry: A new statistical framework for the characterization of white matter pathways, with application to multiple sclerosis. *Hum Brain Mapp.* 2016 Mar;37(3):989-1004. doi: 10.1002/hbm.23082. Epub 2015 Dec 15. PMID: 26667008; PMCID: PMC6867537.
- [55] Bells S, Cercignani M, Deoni S, Assaf Y, Pasternak O, Evans C, Leemans A, Jones D (2011). Tractometry-comprehensive multi-modal quantitative assessment of white matter along specific tracts, in: 17th Annual General Meeting of the British Chapter of the ISMRM.
- [56] De Santis S, Drakesmith M, Bells S, Assaf Y, Jones D (2014): Why diffusion tensor mri does well only some of the time: Variance and covariance of white

- matter tissue microstructure attributes in the living human brain. *NeuroImage* 89:35–44.
- [57] Jones D, Travis A, Eden G, Pierpaoli C, Basser P (2005): Pasta: Pointwise assessment of streamline tractography attributes. *Magn Reson Med* 53:1462–1467.
- [58] Corouge I, Fletcher P, Joshi S, Gouttard S, Gerig G (2006): Fiber tract-oriented statistics for quantitative diffusion tensor mri analysis. *Medical Image Analysis* 10:786–798.
- [59] Maddah M, Grimson W, Warfield S, Wells W (2008): A unified framework for clustering and quantitative analysis of white matter fiber tracts. *Med Image Analysis* 12:191–202.
- [60]
- [61] Cousineau, M., P-M. Jodoin, E. Garyfallidis, M-A. Cote, F.C. Morency, V. Rozanski, M. Grand'Maison, B.J. Bedell, and M. Descoteaux. "A test-retest study on Parkinson's PPMI dataset yields statistically significant white matter fascicles." *NeuroImage: Clinical* 16, 222-233 (2017) doi:10.1016/j.nicl.2017.07.020
- [62] Kurtzer GM, Sochat V, Bauer MW Singularity: Scientific containers for mobility of compute. *PLoS ONE* 12(5): e0177459 (2017) <https://doi.org/10.1371/journal.pone.0177459>
- [63] P. Di Tommaso, et al. Nextflow enables reproducible computational workflows. *Nature Biotechnology* 35, 316–319 (2017) <https://doi.org/10.1038/nbt.3820>
- [64] Song et. al 2022.